



Imperial College London  
Department of Bioengineering

---

# Characterisation of the electrical properties of the human atrium using Physics-Inspired Neural Networks (PINNs)

---

MEng Biomedical Engineering Individual Project – Final Report

Author: Ariele Yehuda Levy Pinto  
CID: 01572402

Supervisor: Dr Marta Varela

Date: 14<sup>th</sup> June 2022

Word Count: 5,990

Submitted in partial fulfilment of the requirements for the award of MEng in Biomedical  
Engineering from Imperial College London

## Abstract

Cardiac arrhythmia, particularly atrial fibrillation (AF), still lacks successful treatments despite being one of the most common diseases globally. It is anticipated that the ability to correctly estimate fundamental electrophysiological (EP) cardiac properties will improve the treatment and diagnosis of arrhythmias like AF by allowing the personalisation of treatment. However, this is not an easy task.

This study proposes Physics-Inspired Neural Networks (PINNs), a novel method for addressing nonlinear problems from limited data, to tackle this issue. The aims are to reproduce action potentials (AP) and estimate relevant EP parameters from the EP cardiac model presented by Fenton et al. [1]. This work shows the EP-PINNs' ability to accurately recreate the AP propagation while estimating EP parameters relevant to AP duration (APD) from synthetically generated data with varying amounts of noise. Finally, the EP-PINNs' performance is also tested on animal in-vitro preparations by describing the influence in APD of anti-arrhythmic drugs (AADs): Nifedipine and E-4031. The results for the synthetic data are excellent, with a mean RMSE of 0.0084 in AP recreation and a 27% mean relative error in EP parameter estimation. For the experimental data, statistically meaningful differences were found in the model parameters between the baseline and experimental measurements in most cases.

This project is a steppingstone to encouraging further research on the applications of PINNs to the diagnosis and treatment of cardiac diseases, especially AF. The complete code and data supporting this study can be found in the following GitHub repository: <https://github.com/arielehlev/EP-PINNs>.

## **Acknowledgements**

First and foremost, I would like to acknowledge and thank my supervisor, Dr Marta Varela. This study would not have been possible without her continuous support, expertise, guidance, and commitment to the project. Her availability, constructive advice, and feedback were key to the successful completion of the project. It has been a pleasure to learn from you.

I am also grateful to my family, partner, friends, and classmates for their continuous support not only through this project but during the past four years.

## Table of Contents

<b>1. Introduction .....</b>	<b>5</b>
1.1. Aims and Objectives.....	5
1.2. Atrial Fibrillation (AF).....	5
1.3. Biophysical Models of Cardiac Electrophysiology .....	7
1.3.1. Cardiac Electrophysiology Background.....	7
1.3.2. Fenton-Karma Model .....	7
1.3.2.1. Estimated Parameters and their Electrophysiological meaning .....	9
1.4. Physics-Inspired Neural Networks (PINNs) .....	10
1.5. Optical Mapping Methods .....	12
<b>2. Methods .....</b>	<b>13</b>
2.1. Data Acquisition.....	13
2.1.1. Synthetic EP Data Generation with Fenton-Karma Model .....	13
2.1.2. Experimental Data .....	13
2.2. EP-PINNs Design and Fenton-Karma Implementation .....	14
2.3. EP-PINNs Implementation for Synthetic Data.....	15
2.3.1. Forward Solution .....	15
2.3.2. Parameter Estimation (Inverse Solution).....	15
2.4. EP-PINNs Implementation for Experimental Data .....	16
2.5. Evaluation.....	17
2.6. Computational Resources .....	17
<b>3. Results.....</b>	<b>18</b>
3.1. Synthetic Data .....	18
3.1.1 Forward Solution .....	18
3.1.2. Parameter Estimation (Inverse Solution).....	21
3.2. Experimental Data .....	22
<b>4. Discussion: .....</b>	<b>24</b>
4.1. Synthetic Data .....	24
4.1.1. Forward Solution .....	24
4.1.2. Parameter Estimation (Inverse Solution).....	25
4.2. Experimental Data .....	25
4.3. Further Improvements .....	26
<b>5. Conclusion .....</b>	<b>27</b>
<b>6. References .....</b>	<b>28</b>

# 1. Introduction

## 1.1. Aims and Objectives

Herrero Martin et al. (2022) show that EP-PINNs succeed in solving the monodomain Aliev-Panfilov model, a model representing both the restitution properties of the heart and an accurate AP shape [2]. They show that EP-PINNs successfully estimate APD-related parameters. However, this simple model (only six parameters) does not fully capture the behaviour of specific ionic currents and channels, which is essential to characterise the actions of AADs [3]. This study therefore presents the more complex three-current ionic EP model (15 parameters) proposed by Flavio Fenton and Alain Karma and integrates it with EP-PINNs [1].

This project aims to characterise changes in EP properties induced by AADs, using PINNs trained on the Fenton-Karma cardiac mathematical model. This would help design strategies for treatment of AF. Accordingly, we use the PINNs framework to achieve the following objectives:

1. Solve the equations of the Fenton-Karma cardiac model using synthetically generated data.
2. Estimate meaningful EP parameters using synthetically generated data.
3. Estimate meaningful EP parameters from experimental data to discover detailed AAD effects.

We hypothesise that the Fenton-Karma model's thorough characterisation of current flowing through ionic channels, paired with PINNs, will bring us closer to personalising AAD selection than the Aliev-Panfilov model, thereby increasing the efficacy of therapy for arrhythmias, including AF.

## 1.2. Atrial Fibrillation

Cardiac arrhythmias are pathological irregularities in heart rhythm, produced by disruptions in the electrical impulses driving the heartbeat [4]. They are found in >2% of the population, making it one of the commonest conditions worldwide [5]. The commonest arrhythmia is AF, which accounts for ~43% of all cardiac arrhythmias [6]. AF is more likely to develop with increasing age; its incidence is anticipated to double in the next few decades [7]. AF commonly impairs quality of life considerably [8]. It is linked to higher risk of stroke and other diseases, resulting in a 1.5-fold mortality risk in men and 1.9-fold risk in women [9].

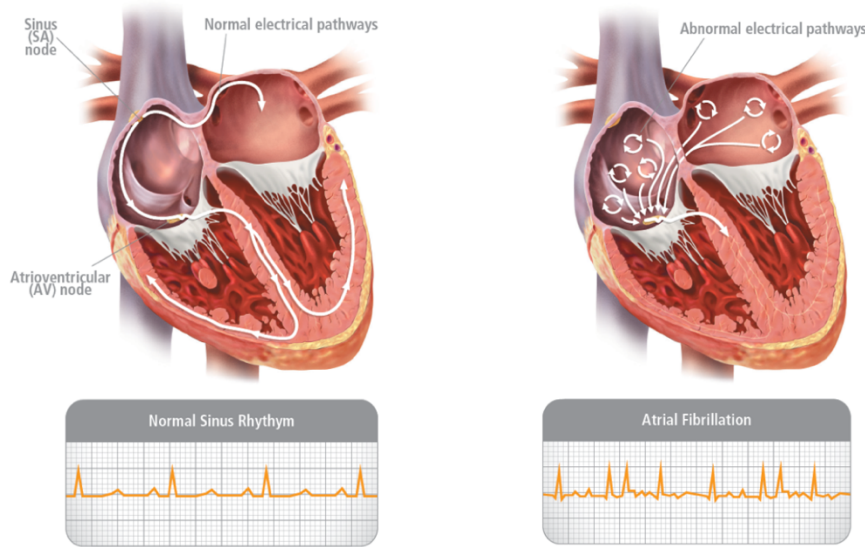


**Figure 1.1:** Healthy heart with regular sinus rhythm (left) vs AF with disorganised signals in the atria (right) complemented by characteristic electrocardiographic signals from both [10].

The highly complex dynamics of AF are still not fully understood despite extensive investigation [11]. This condition is characterised by cluttered signals in the atria (Figure 1.1). Consequently, the atrioventricular node becomes overburdened with electrical impulses seeking to reach the ventricle, causing a fast and uneven pulse [12].

Cardioversion therapy, surgery, and pharmaceuticals, such as AAD regimens, are the main treatments for AF [7]. Nevertheless, the most frequent and arguably the most successful is catheter ablation. This procedure uses energy to create millimetric scars in the heart tissue to block atypical electrical signals, preventing them from propagating through the heart [13]. However, the long-term success rate of this treatment in patients with longstanding AF is only 54% [14] as it is difficult to identify suitable locations to perform the ablation [15]. Moreover, it is a very expensive procedure, with a median cost of \$32,756 per patient [16].

To increase life expectancy and reduce the socio-economic burden of treating this disease, researchers are exploring potential treatments such as AAD therapy. Traditional AAD therapy has a success rate of 30%-60%, with no drug showing superior results [17], partly due to lack of knowledge of AF's origin and progression mechanisms [18]. The main reason for these poor success rates is that no standard mechanism defining arrhythmias exists; they differ considerably between patients, leading to faulty drug selection [17]. Current AAD treatment is not personalised; pharmacological activity on cardiac tissue is thought to be consistent across different patients. A method is required to assess personalised drug effects using multicellular experimental data including sufficient detail of which ion channels are affected, as both catheter ablations and AADs might be more successful if adapted to the patient.

## 1.3. Biophysical Models of Cardiac Electrophysiology

### 1.3.1. Cardiac Electrophysiology Background

Studies suggest that areas with irregular electrical activity causing arrhythmias frequently display atypical EP characteristics [19]. Extensive EP characterisation is required to better understand how AF impacts heart rhythm. To achieve this, we develop a mathematical model of the heart and use computational tools (PINNs) to derive its EP characteristics.

First, we examine how the heart functions. Electrical signals travelling across the heart trigger the atria and ventricles to contract. A typical membrane potential throughout a single AP is shown in Figure 1.2, along with the ion fluxes influencing it at each phase. Activation of voltage-gated ion channels induces depolarisation of the myocyte's membrane, culminating in an inflow of  $\text{Na}^+$  (Phase 0) and eventually  $\text{Ca}^{2+}$  (Phases 1 and 2), stimulating heart-muscle contraction [20]. The membrane undergoes early repolarisation due to the outflow of mainly  $\text{K}^+$  (Phase 1) [21]. Inflow of  $\text{Ca}^{2+}$  restores equilibrium resulting in a plateau state (Phase 2). Finally, a  $\text{K}^+$  outflow causes final repolarisation (Phase 3). A cardiac AP comprises a single cycle of depolarisation and repolarisation, lasting 200 milliseconds on average in the atria [22]. The initial AP is generated by pacemaker cells, and is subsequently transmitted to adjacent cardiac cells through gap junctions [23].

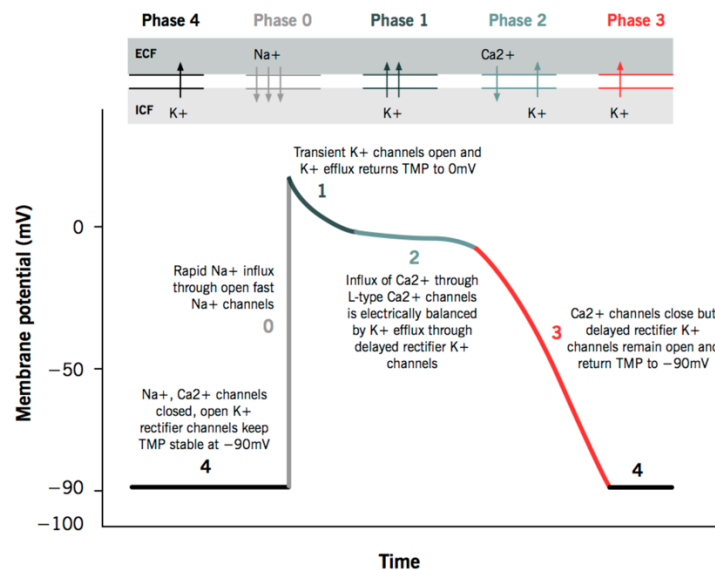


**Figure 1.2:** AP of cardiac muscles. ICF and ECF denote intracellular and extracellular fluid respectively [24].

### 1.3.2. Fenton-Karma Model

To characterise the action of AADs, a thorough cardiac model must be used, providing information about individual ion currents and channels relevant to cardiac behaviour. Fenton and Karma's three-current ionic model (1998) includes reasonable estimates of cardiac restitution characteristics [1]. Their model seeks to quantitatively recreate the restitution characteristics specifying how pulse period and propagation velocity are affected during the period following repolarisation. This occurs, however, by maintaining the bare minimum of

ionic complexity. These attributes are included in our model, with a value  $I_{ion}$  representing the sum of three separate currents.

$$I_{ion} = I_{fi}(u; v) + I_{so}(u) + I_{si}(u; w) \quad (1.1)$$

The three currents are defined as follows: (i)  $I_{fi}$  is a “fast inward current” behind depolarisation. It is driven by  $v$ , which activates  $I_{fi}$  after repolarisation and inactivates it after depolarisation. (ii)  $I_{so}$  reflects a “slow outward current” driving membrane repolarisation. Finally, (iii)  $I_{si}$ , “slow inward current”, balances  $I_{so}$  bringing the AP to its plateau phase. It is controlled by  $w$ , a gating variable that activates  $I_{so}$  [1].

The currents  $I_{fi}$ ,  $I_{so}$ , and  $I_{si}$  are homologous to the  $\text{Na}^+$ ,  $\text{K}^+$ , and  $\text{Ca}^{2+}$  currents. They are not identical as the dynamics of the membrane are far more complicated than the ionic oversimplified currents displayed above. However, this model does not seek to represent the  $\text{Na}^+$ ,  $\text{K}^+$ , and  $\text{Ca}^{2+}$  currents perfectly, but to describe cardiac membrane restitution characteristics with only the necessary ionic complexity. Expanding further into the model, membrane potential is specified by the dimensionless factor  $u$ , with a value between 0 and 1, defined by Equation 1.2.

$$u \equiv \frac{(u - u_o)}{u_{fi} - u_o} \quad (1.2)$$

**Equation 1.2:** Definition of membrane potential ( $u$ ).  $u_o$  refers to the resting membrane potential.  $u_{fi}$ , the potential at which the fast inward current has no net flow, corresponds approximately to the maximum value of  $u$  during the AP [1].

The equations for the three scaled currents, fast inward, slow outward, and slow inward, are the following:

$$J_{fi} = I_{fi} / (C_m(V_{fi} - V_o)) \quad (1.3)$$

$$J_{so} = I_{so} / (C_m(V_{so} - V_o)) \quad (1.4)$$

$$J_{si} = I_{si} / (C_m(V_{si} - V_o)) \quad (1.5)$$

**Equations 1.3 – 1.5:** Definition of the fast inward-scaled current  $J_{fi}$ , the slow outward-scaled current  $J_{so}$ , and the slow inward-scaled current  $J_{si}$ . The membrane’s capacitance is represented as  $C_m$ . The Nernst potential of the slow outward and slow inward currents are represented by  $V_{so}$  and  $V_{si}$ , respectively [1].

The model is represented as Equations 1.6 – 1.8, with the three ionic currents corresponding to Equations 1.9 – 1.11. The flow of  $u$  between adjacent cells through gap junctions appears in Equation 1.6. It is expressed in the monodomain model, which assumes equivalent anisotropy in intracellular and extracellular spaces (i.e., extracellular and intracellular conductivity proportional to one another) [25]. Equation 1.6 assumes AP propagation is isotropic and homogeneous. Thus the diffusion term  $\nabla \cdot (\tilde{D} \nabla u)$  simplifies to  $\tilde{D} \nabla^2 u$ .  $\tilde{D}$  is the diffusion tensor, reflecting how quickly  $u$  may disseminate and become more



homogeneous in space, making it a key determinant of AP propagation velocity. It's directly proportional to myocardial electrical conductivity [2].  $v$  activates and deactivates  $I_{fi}$ , and  $w$  is a recovery variable, governing the model's restitution and refractoriness features, leaving no diffusion term in these channels [1].

$$\partial_t u = \nabla \cdot (\tilde{D} \nabla u) - J_{fi}(u; v) - J_{so}(u) - J_{si}(u; w) \quad (1.6)$$

$$\partial_t v = \Theta(u_c - u)(1 - v)/\tau_v^-(u) - \Theta(u - u_c)v/\tau_v^+ \quad (1.7)$$

$$\partial_t w = \Theta(u_c - u)(1 - w)/\tau_w^- - \Theta(u - u_c)v/\tau_w^+ \quad (1.8)$$

**Equations 1.6 – 1.8:** Fenton-Karma model Equations.  $\Theta(x)$ , the Heaviside function, returns  $\Theta(x) = 1$  for a positive input ( $x \geq 0$ ), and  $\Theta(x) = 0$  for a negative one ( $x < 0$ ).

$$J_{fi}(u; v) = -\frac{v}{\tau_d} \Theta(u - u_c)(1 - u)(u - u_c) \quad (1.9)$$

$$J_{so}(u) = \frac{u}{\tau_o} \Theta(u_c - u) + \frac{1}{\tau_r} \Theta(u - u_c) \quad (1.10)$$

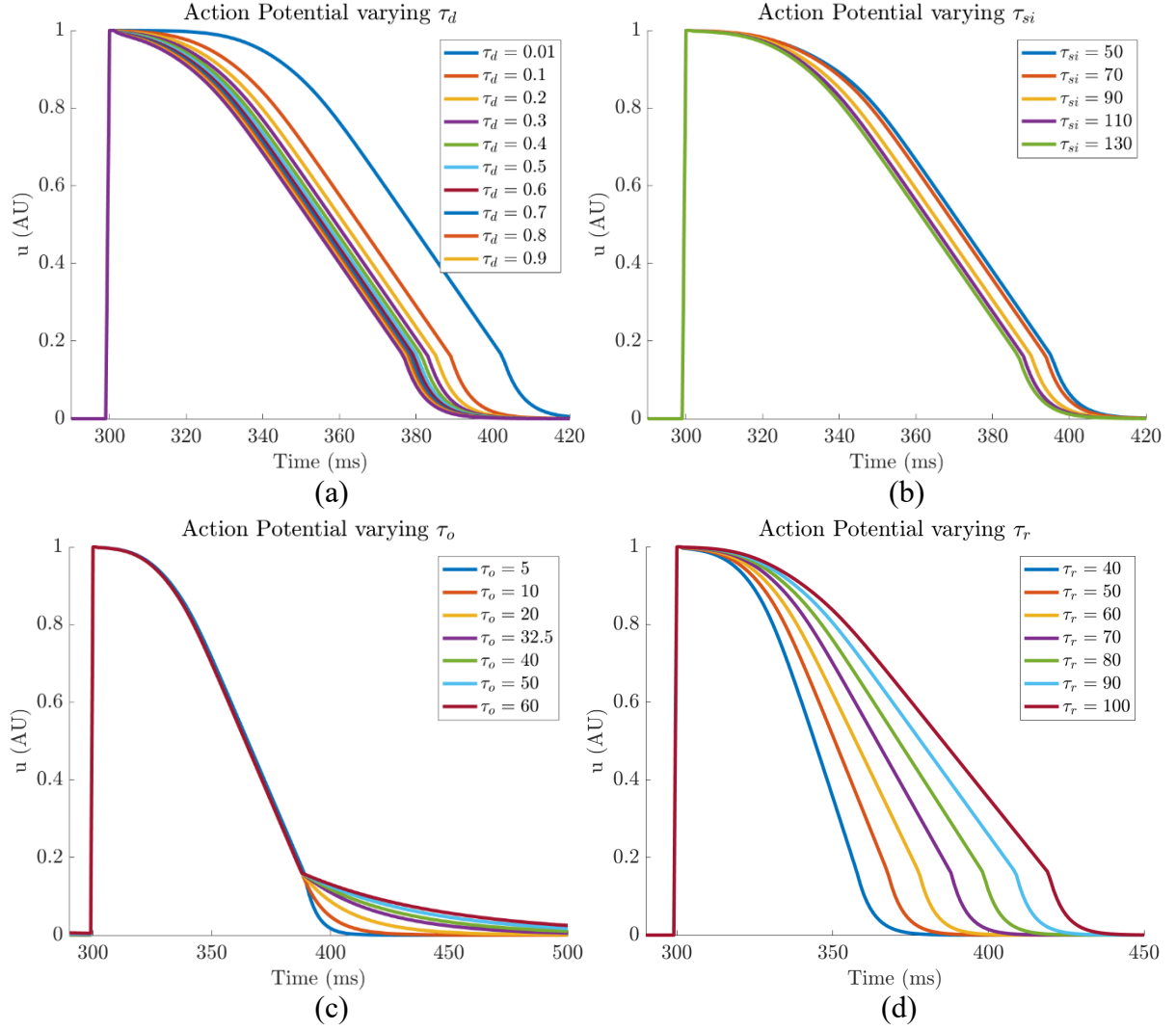
$$J_{si}(u; w) = -\frac{w}{2\tau_{si}} (1 + \tanh[k(u - u_c^{si})]) \quad (1.11)$$

**Equations 1.9 – 1.11:** The three ionic currents [1].

Solving the above equations for each individual, characterising patients' EP properties, is key to individualising AAD selection to increase the efficacy of arrhythmia therapies, in this case, AF. Nevertheless, the model parameters (i.e.,  $\tau_d$ ,  $\tau_o$ ,  $\tau_r$ ,  $\tau_{si}$ ) differ between individuals and cardiac regions and when diseases or AADs are present. PINNs offer a tool to estimate these parameters from biological signals without requiring exorbitant computational resources or trial-and-error methods.

### 1.3.2.1. Estimated Parameters and their Electrophysiological meaning

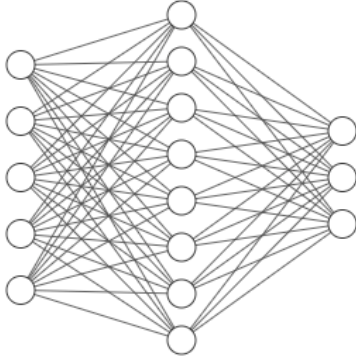
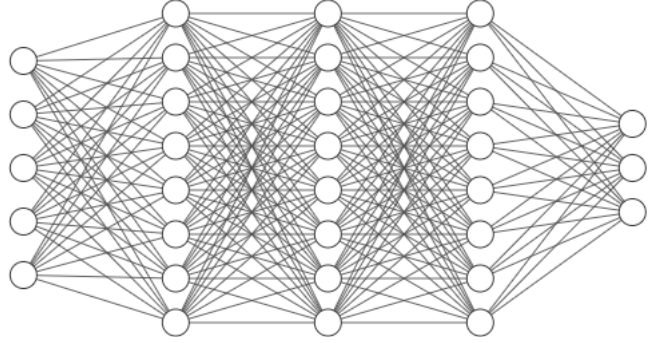
The parameters estimated by the EP-PINNs are the diffusion coefficient  $D$  and the Fenton-Karma parameters  $\tau_d$ ,  $\tau_o$ ,  $\tau_r$ , and  $\tau_{si}$ , which directly affect the  $J_{fi}(u; v)$ ,  $J_{so}(u)$  and  $J_{si}(u; w)$  currents, analogous to the  $\text{Na}^+$ ,  $\text{K}^+$ , and  $\text{Ca}^{2+}$  currents influencing heart rhythm. To better understand how these parameters affect APD, Figure 1.3 shows how Fenton-Karma AP simulations were run for a range of values of these parameters, revealing that varying these parameters either shortens or prolongs the AP differently. Some shorten/extend the plateau phase ( $\tau_d$  and  $\tau_{si}$ ); others shorten/lengthen the repolarisation phase ( $\tau_o$  and  $\tau_r$ ). They do this in different ways (Figure 1.3).



**Figure 1.3:** Action Potentials for varying  $\tau_d$  (a),  $\tau_{si}$  (b),  $\tau_o$  (c), and  $\tau_r$  (d).

#### 1.4. Physics-Inspired Neural Networks (PINNs)

90% of the global data was created between 2016 and 2018 [26]. Due to exponentially rising rates of data generation, advanced computational methods are required to conduct, among others, classification and pattern recognition tasks from massive volumes of data. Hence, machine learning (ML) approaches, especially its subfield deep learning, characterised by deep artificial neural networks, are increasingly popular. Artificial neural networks (NNs) are a subset of ML, comprising interconnected nodes that imitate the human brain, each with its own weight and bias [27]. A NN must have more than one hidden layer to be considered "deep" (Figure 1.4) [28].

**Artificial Neural Network****Deep Artificial Neural Network****Figure 1.4:** Difference between a simple and a deep Artificial NN [29].

NNs have demonstrated excellent accuracy in numerous classification and pattern-recognition problems. Nevertheless, to produce acceptable results, NNs must be trained on extensive, high-quality datasets and use a significant number of computer resources. From a clinical standpoint, obtaining large quantities of high-quality data is hampered by privacy concerns and technology restrictions, making data collection costly and occasionally invasive. PINNs leverage previous knowledge of physical principles of the system we wish to investigate to limit possible solutions to a manageable level. This enables the network to train with less data than standard NNs, requiring fewer computational resources without affecting accuracy [30].

Understanding of the system dynamics is integrated by inserting partial differential equations (PDEs) and ordinary differential equations (ODEs) that describe the system's behaviour (Equations 1.6 – 1.8). Each task has distinctive initial and boundary conditions and other properties naturally enforced by the PINNs. To compute the terms of the PDEs, the PINNs construct a minimisation function based on residuals utilising established automated differentiation methods. Equation 1.12 below shows a general PDE system.

$$\frac{\partial u}{\partial t} = F(u(x, t); \lambda), \quad x \in \Omega, \quad t \in [0, T] \quad (1.12)$$

**Equation 1.12:** Generic PDE.  $u(x, t)$  is the latent solution;  $\lambda$  represents parameters of the dynamics.

PINNs can solve two types of optimisation task: (i) When all the model's parameters ( $\lambda$ ) are known, the PINNs train the NN parameters to approximate the latent solution  $u(x, t)$ , hence mimicking the system's behaviour (in this case, AP propagation). Here the PINNs run in forward mode. (ii) By obeying the provided PDE and data, the PINNs determine the solution  $u(x, t)$  and estimate the parameters  $\lambda$ . This is the parameter estimation task, and the PINNs operate in inverse mode.

Equation 1.13 describes the EP-PINN loss function. The first three terms relate to data agreement and initial and Neumann boundary conditions. These are minimised with supervised learning. The last term, which is unsupervised and distinguishes the PINNs, relates to the problem's physics, and will increase if the NN's outcome does not respect the system dynamics. The definition of individual losses is shown in Equations 1.14 – 1.17 below.

$$L = L_{data} + L_{IC} + L_{BC} + L_f \quad (1.13)$$

**Equation 1.13:** EP-PINN loss function. Subscripts  $f$ ,  $data$ ,  $IC$ , and  $BC$  correspond to physical laws, observed data agreement, initial condition and boundary condition, respectively.

$$L_{data} = \frac{1}{N} \sum_{n=1}^N (\tilde{u}(x_n, t_n) - u(x_n, t_n))^2 \quad (1.14)$$

**Equation 1.14:** Observed data agreement loss.

$$L_f = \frac{1}{N} \sum_{n=1}^N (\tilde{f}_u(x_n, t_n)^2 + \tilde{f}_v(x_n, t_n)^2 + \tilde{f}_w(x_n, t_n)^2) \quad (1.15)$$

**Equation 1.15:** Physical-laws consistency loss. The three squared terms correspond to the terms in Equations 2.1 – 2.3, outlined in the methods section.

$$L_{IC} = \frac{1}{N_{ic}} \sum_{n=1}^{N_{ic}} (\tilde{u}(x_n, 0) - u(x_n, 0))^2 \quad (1.16)$$

**Equation 1.16:** Initial condition loss.  $N_{ic}$  corresponds to the number of points at  $t = 0$ .

$$L_{BC} = \frac{1}{N_{bc}} \sum_{n=1}^{N_{bc}} \left( \frac{\partial \tilde{u}}{\partial \vec{n}}(x_n, t_n) \right)^2 \quad (1.17)$$

**Equation 1.17:** Boundary condition loss.  $N_{bc}$  corresponds to the number of data points conforming to the Neumann boundary conditions.

## 1.5. Optical Mapping Methods

Optical mapping evaluates transmembrane voltage and employs voltage-sensitive fluorescent dyes and a camera with high spatiotemporal resolution [31]. In-vitro optical mapping studies provide accurate insights into AP features and single-cell EP characteristics, yet in vivo this is challenging. Optical mapping techniques can investigate the influence of AADs on cardiomyocyte preparations [32]. Therefore, to evaluate EP-PINNs in an experimental environment, these will be assessed with optical mapping data from newborn rat ventricular myocytes samples stained with a voltage-sensitive dye [32].

## 2. Methods

### 2.1. Data Acquisition

#### 2.1.1. Synthetic EP Data Generation with Fenton-Karma Model

The synthetic data comprising the ground truth (GT) for this experiment was created in MATLAB using central finite differences and a 4-stage Runge-Kutta method to solve the Fenton-Karma model. An electrical wave was set to propagate along a 1D 100-cell cable. The first five cells were initialised with a  $u = 1.0 AU$  for  $1 ms$  at one side of the cable. This initiated a planar wave that propagated onto the neighbouring cells. The simulation is  $150 ms$  long with a step of  $0.005 ms$ . Cell length was  $0.1 mm$  (producing a 1D cable of  $1 cm$ ) and a diffusion coefficient of  $D = 0.1 mm^2/ms$  was used. Using a fixed value for  $D$ , the conduction is modelled as isotropic and homogeneous. Table 1 below shows the values used in the Fenton-Karma model, chosen to make the APs resemble atrial ones [33]. Neumann boundary conditions were implemented, enforcing no net flow of current perpendicular to the heart’s tissue boundary (i.e.,  $\frac{\partial u}{\partial n} = 0$  in the cable’s boundary) [1]. This prevents  $u$  leaking beyond the cardiac domain [2].

Parameter	Value	Parameter	Value
$u_v$	0.16	$\tau_{v2}$	60
$u_w$	0.16	$\tau_{v+}$	5.75
$u_u$	0.16	$\tau_o$	32.5
$u_{vsi}$	0.04	$\tau_w^-$	400
$u_{csi}$	0.85	$\tau_w^+$	300
$k$	10	$\tau_r$	70
$\tau_d$	0.125	$\tau_{si}$	114
$\tau_{v1}$	82.5		

**Table 1:** Fenton-Karma parameters [33].

#### 2.1.2. Experimental Data

For real-world validity, the EP-PINNs must be empirically tested. Optical mapping methods recorded data from newborn rat ventricular myocardial preparations stained with a voltage-sensitive dye. This experiment was performed by Chowdhury et al., who kindly offered access to their data [32]. The Ethical Committee of Imperial College London approved the animal data-collection methods in compliance with EU Directive 2010/63/EU standards [32].

The optical mapping data comprises a longitudinal collection of 2D spatial images. Following some pre-processing, the resulting signal was averaged to improve the signal-to-noise ratio as described by Herrero Martin et al. (2022) [2].

The potential across the cells was recorded for two scenarios: resting (baseline) and influenced by two simulated AADs, Nifedipine and E-4031, chosen because of their opposite effect on APD; each blocks, respectively, the L-type calcium channel ( $I_{CaL}$ ) and hERG voltage-

gated potassium channel ( $I_{Kr}$ ) [2]. E-4031 extends APD while Nifedipine shortens it. These effects should be identified as decreases in the Fenton-Karma  $I_{so}$  and  $I_{si}$  currents, respectively.

## 2.2. EP-PINNs Design and Fenton-Karma Implementation

The EP-PINNs were programmed with the help of the Python DeepXDE library, which facilitates the implementation of such NNs [34]. DeepXDE's kit solves ODEs/PDEs in forward and inverse mode with PINNs [34]. It allows the user to call these functions with parameters of their choice, an appropriate framework for this project.

The PINN chosen to solve our model is a feed-forward, fully connected neural network (FNN) with two input nodes for the space and time positions and three output nodes for  $u$ ,  $v$ , and  $w$  (Figure 2.1). The training was constrained by the Fenton-Karma model's system dynamics, implemented as the following functions (Equations 2.1 – 2.3) after rearrangement of Equations 1.6 – 1.8. The network is trained to satisfy these equations with observable data gathered synthetically or experimentally.

$$f_u(x, t) = \partial_t u - \nabla \cdot (\tilde{D} \nabla u) + J_{fi}(u; v) + J_{so}(u) + J_{si}(u; w) \quad (2.1)$$

$$f_v(x, t) = \partial_t v - \frac{\Theta(u_c - u)(1 - v)}{\tau_v^-(u)} + \frac{\Theta(u - u_c)v}{\tau_v^+} \quad (2.2)$$

$$f_w(x, t) = \partial_t w - \frac{\Theta(u_c - u)(1 - w)}{\tau_w^-} + \frac{\Theta(u - u_c)v}{\tau_w^+} \quad (2.3)$$

**Equations 2.1 – 2.3:** Equations of the model where  $\Theta(x)$  is the Heaviside function.

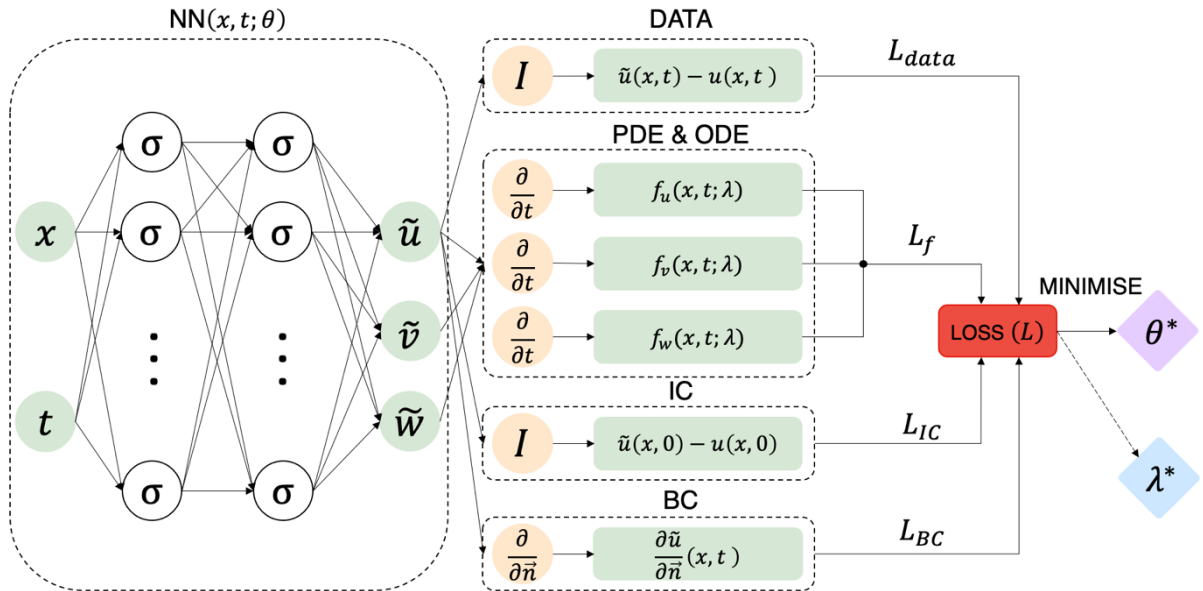


**Figure 2.1:** EP-PINN architecture following the Fenton-Karma model. In forward mode, it optimises the weights  $\theta$  to approximate the solution  $u(x, t)$ , solving solve the PDE-ODE system. In inverse mode, it also estimates parameters  $\lambda$ .

## 2.3. EP-PINNs Implementation for Synthetic Data

### 2.3.1. Forward Solution

The EP-PINNs first solved the equations in forward mode. A FNN with 4 hidden layers of 32 neurons each was trained for 60k epochs with a learning rate  $lr = 5 \times 10^{-4}$ , a  $\tanh$  activation, a Glorot Uniform initialiser, and Adam optimisation. The following experiments evaluated the network's stability and reliability, solving forward problems in various circumstances.

#### Left and Right Initialisation

The heart comprises many cells, so performance should be invariant regardless of the initialisation's origin, ensuring system symmetry. Therefore, the network was trained with datasets with initialisations from the left and right sides of the cable. This was done by initialising the five left cells for one dataset and the five right ones for the other. The experiment was repeated ten times for each initialisation. A left initialisation was used for the remaining experiments.

#### Addition of Noise

To better mimic actual heart conditions, the EP-PINNs were evaluated in the presence of noise. Therefore, random zero-mean Gaussian noise was introduced to  $u_{GT}$ . Experiments with the standard deviations ( $\sigma$ ) below were run. 1  $AU$  is the characteristic peak amplitude of the action potential.

$$\sigma = \{0, 0.02, 0.05, 0.07, 0.1, 0.15, 0.2, 0.25, 0.3, 0.35, 0.4, 0.45, 0.5, 0.6, 0.7, 0.8, 0.9\} AU$$

#### Data Points Reduction

Access to medical data is usually restricted by financial, time, equipment, or privacy circumstances. Thus, the performance of the EP-PINNs with access to fewer data points was investigated. The EP-PINN was trained with the following data points ( $N$ ) for this experiment. The remaining experiments were run with only 1500 data points, corresponding to just 10% of data available for training.

$$N = \{12000, 7500, 4500, 1500, 750, 150, 75, 60, 45, 30, 15, 10, 7, 4, 1\}$$

#### Restrictions to $f_v$ and $f_w$ losses.

The network is constrained by physical laws through the losses of  $f_u$ ,  $f_v$ , and  $f_w$ . However, it is interesting to investigate if EP-PINNs give physically plausible estimates with only access to  $f_u$ . If so, a simpler model would reduce the burden to the network, accelerating training, and cutting data requirement.

### 2.3.2. Parameter Estimation (Inverse Solution)

To complete parameter estimation, the EP-PINN must be run in inverse mode. Here, the user will not provide fixed values for some parameters. These will be set as variables, initialised appropriately, that the EP-PINN will estimate during training [34].

Four parameters were inferred individually by the EP-PINNs and in pairs:  $\tau_d, \tau_r, \tau_o, \tau_{si}$ , and diffusion coefficient  $D$ . These were chosen for their physiological meaning.  $\tau_d$  controls  $J_{fi}(u; v)$ ,  $\tau_r$  and  $\tau_o$  affect  $J_{so}(u)$ ,  $\tau_{si}$  affects  $J_{si}(u; w)$ , and  $D$  affects the conduction velocity (Equations 1.9 – 1.11). A FNN was trained for 100k epochs with a learning rate of  $lr = 5 \times 10^{-5}$ , a  $\tanh$  activation, a Glorot Uniform initialiser, and Adam optimisation. The architecture varied according to the parameters estimated (Table 2).

Parameter	Number of Hidden Layers	Size of Hidden Layers
$\{D\}, \{\tau_{si}\}, \{\tau_{si}, D\}$	5	32
$\{\tau_d\}, \{\tau_d, D\}$	4	32
$\{\tau_o\}, \{\tau_o, D\}$	5	16
$\{\tau_r\}, \{\tau_r, D\}$	6	32

**Table 2:** Network architecture for parameter estimation.

## 2.4. EP-PINNs Implementation for Experimental Data

This study aims to estimate parameters during training from experimental AAD measurements. The experimental data is pre-processed, so the resulting dataset is 1D, representing two cells close in time [2]. Therefore, the network architecture is the same as for the synthetic data. Two experiments evaluated the performance of the EP-PINNs with experimental data:

1. Parameter  $\tau_{si}$  was estimated for data under the effects of Nifedipine and baseline measurement. This is because Nifedipine blocks the L-type calcium channel ( $I_{CaL}$ ), and the  $\text{Ca}^{2+}$  current is homologous to  $I_{si}$ , which is affected by  $\tau_{si}$ . Estimation of  $\tau_{si}$  will be observed, as an elevated  $\tau_{si}$  reduces APD in comparison to the baseline. Thus, we formulate the hypothesis below. The other parameters should remain unchanged.

$$H_0: \tau_{si} (\text{baseline}) = \tau_{si} (\text{drug active})$$

$$H_a: \tau_{si} (\text{baseline}) < \tau_{si} (\text{drug active})$$

2. Parameters  $\tau_r$  and  $\tau_o$  were estimated for data under the effects of E-4031 and baseline measurements. E-4031 blocks the hERG voltage-gated potassium channel ( $I_{Kr}$ ). The  $\text{K}^+$  current is homologous to  $I_{so}$ , which increases with elevated  $\tau_r$  and  $\tau_o$  values, resulting in a longer APD compared to baseline, prompting the hypothesis below. The other parameters should remain unchanged.

$$H_0: \tau_r/\tau_o (\text{baseline}) = \tau_r/\tau_o (\text{drug active})$$

$$H_a: \tau_r/\tau_o (\text{baseline}) < \tau_r/\tau_o (\text{drug active})$$

To evaluate the hypothesis, a one-tailed t-test [35] is performed on the values of interest with a significance level of 0.05 ( $p < 0.05$ ). To check whether the other parameters remained unchanged with respect to the baseline, a two-tailed t-test is performed to detect whether the means are different with a significance level of 0.05;  $p > 0.05$  suggesting no difference.



Finally, quantitative measurements of APD to compare the results are needed. One, known as APD90, is the time in *ms* taken between the AP rise (maximum value) and drop to 90% of that value. The next, APD50, is identical, but measures the time (*ms*) taken to drop to 50% of maximum value. The last is needed in case of a change in shape (a longer plateau phase followed by a steep fall). APD90 would capture this as a longer APD than APD50. Thus, both measurements should be considered.

## 2.5. Evaluation

In forward mode, since the EP-PINNs predict solutions for  $u$ , the root mean square error (RMSE) is computed to evaluate the accuracy of  $u$  estimations (Equation 2.9). In inverse mode, model parameters are also estimated; apart from the RMSE error in  $u$ , a relative error (RE) will be calculated between the estimated and reference parameters (Equation 2.10). Illustrations of the predicted APs are provided in most cases to observe how well the predicted solution fits the GT data. Finally, the t-tests are employed to evaluate the changes in ionic characteristics caused by pharmacological effects in the experimental data. The experiments were run five times, unless specified otherwise, to account for variability.

$$RMSE = \sqrt{\frac{1}{N_{test}} \sum_{i=1}^{N_{test}} (u(i) - u_{GT}(i))^2} \quad (2.9)$$

**Equation 2.9:** Equation for RMSE.  $N_{test}$  is the number of test points.

$$RE = \frac{\theta_{true} - \theta_{estimated}}{\theta_{true}} \quad (2.10)$$

**Equation 2.10:** Equation for RE.  $\theta$  denotes the parameter estimated during training.

## 2.6. Computational Resources

The training of the EP-PINNs was completed using a 12GB NVIDIA Tesla K80 GPU and 2 Intel® Xeon® CPUs @ 2.20 GHz. The average standard training time for 100k epochs is 18 minutes. 60k epochs trainings took approximately 10 minutes.

### 3. Results

#### 3.1. Synthetic Data

##### 3.1.1 Forward Solution

###### Left and Right Initialisation

Figure 3.2 shows how the EP-PINNs estimated the forward solution of the Fenton-Karma model compared to the GT data provided for initialisations on the left- and right-hand sides of the cable. RMSE results for the forward solution in 10 repetitions were  $RMSE = 0.0098 \pm 0.0026$  for the left initialisation, and  $RMSE = 0.0107 \pm 0.0036$  for the right.

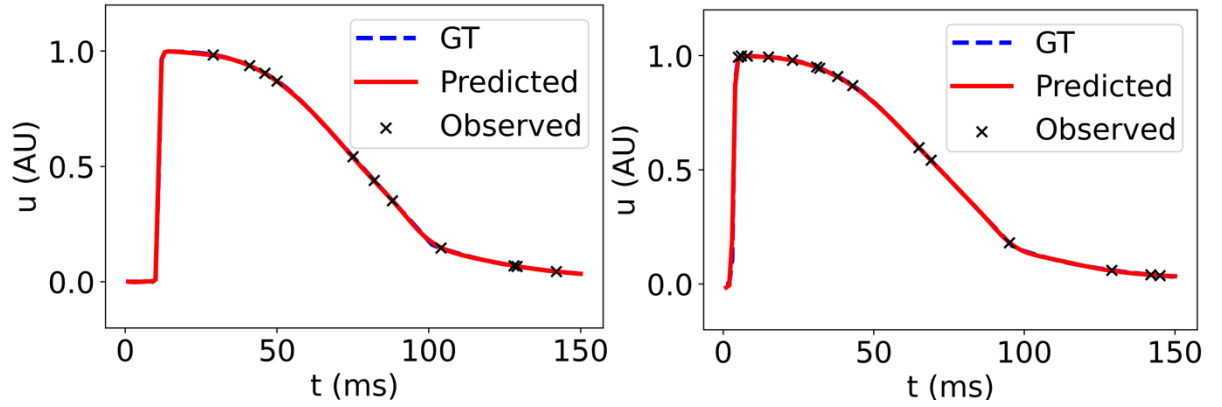


**Figure 3.2:** EP-PINN's forward solution of the Fenton-Karma model showing predicted and GT APs with left-side (left) and right-side (right) initialisations.

###### Addition of Noise

Introducing noise generated RMSE variations. Figure 3.3 shows how RMSE (mean  $\pm$  sd) changed as a function of the noise and includes illustrations of the predicted APs. The RMSE remains approximately constant until  $\sigma = 0.1$ , then increases roughly linearly until  $\sigma = 0.6$ , finally increasing more abruptly until  $\sigma = 0.9$ , where the EP-PINN seems no longer to converge to the solution.

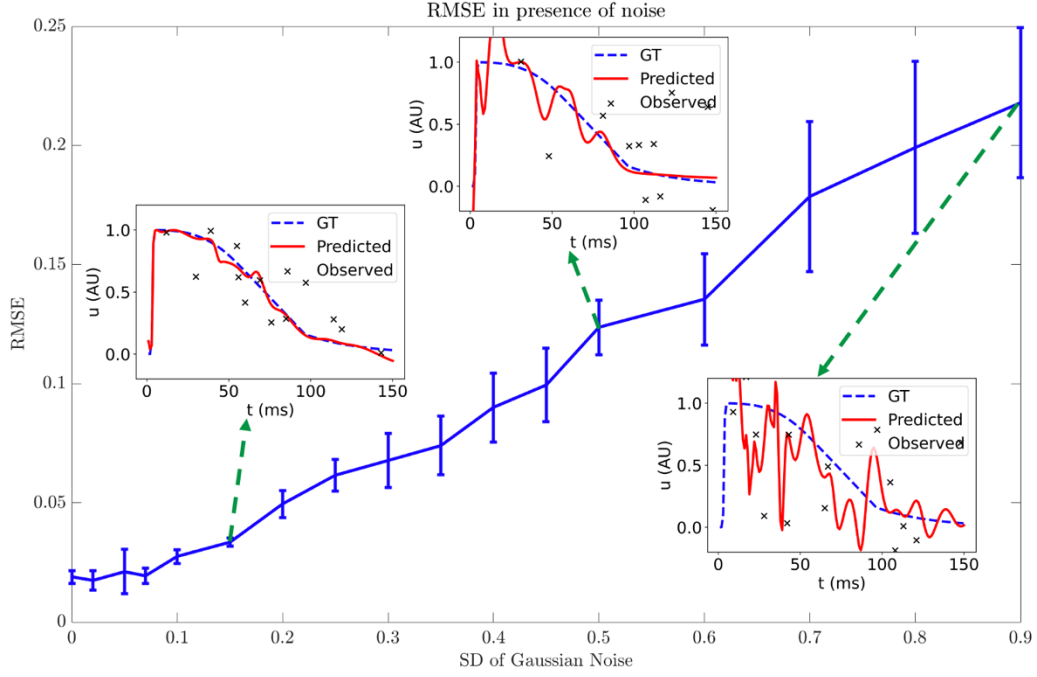


**Figure 3.3:** RMSE as a function of noise level. Predicted AP plots are included for noises of  $\sigma = \{0.15, 0.5, 0.9\}$ .

### Data Point Reduction

Figure 3.4 illustrates the forward model's RMSE (mean  $\pm$  sd) when varying the number of observed sampled points. Graphs showing predicted APs for some cases are included. The RMSE is almost invariant when trained with datapoints ranging between 12000-750. A slight increase around  $10^2$  datapoints follows. Finally, it explodes exponentially until reaching one training datapoint where predicted the AP is far from fitting the GT data.

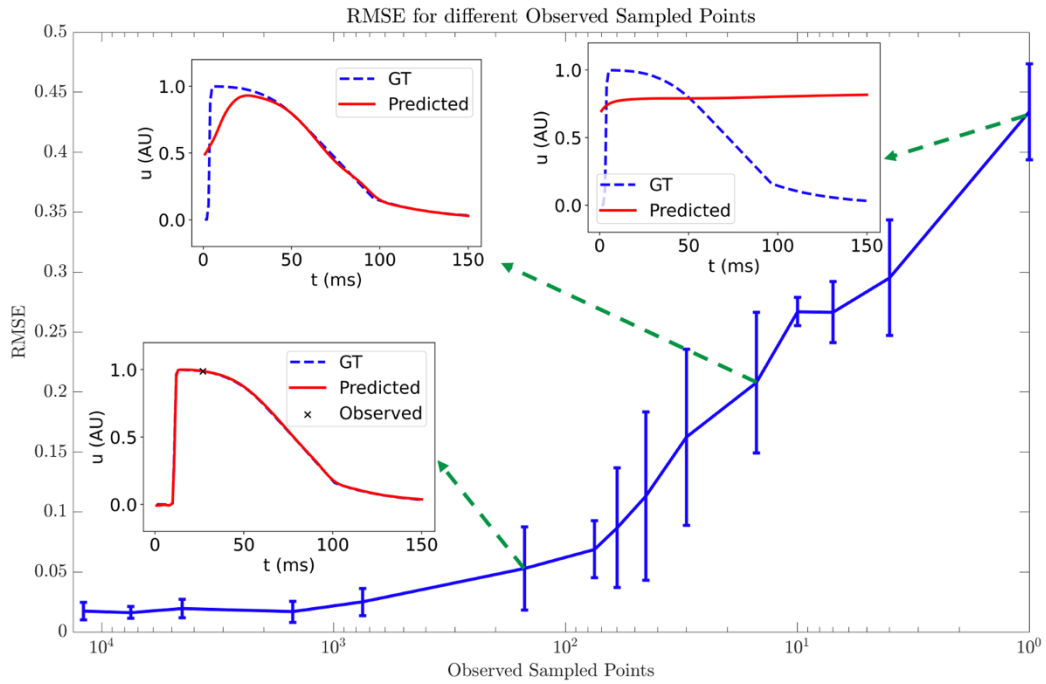


**Figure 3.4:** RMSE as a function of the number of observed sampled points. Predicted AP plots are included for  $N = \{150, 15, 1\}$ .

### Restrictions to $f_v$ and $f_w$ losses

The network was trained without the  $f_v$  and  $f_w$  losses (Equation 1.15), and its performance compared to that of the full model. The RMSE (mean  $\pm$  sd) results appear in Figure 3.5. In both experiments, the RMSE of the reduced model (restricted to  $f_v$  and  $f_w$  losses) is comparable to that of the full model with a few exceptions at extremely high noise levels and very low sampling points quantity. Training time was reduced by over 20% with the reduced model.

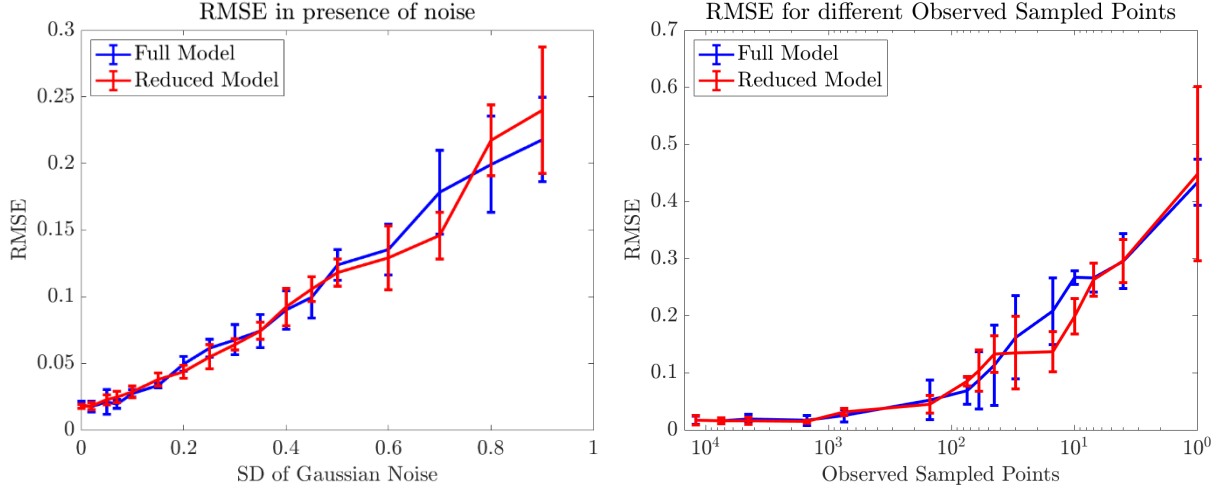


**Figure 3.5:** Comparison of RMSE as a function of noise level (left) and observed sampled points (right) between full and reduced model.

Figure 3.6 illustrates how well the EP-PINNs fit  $v$  and  $w$  with and without access to the  $f_v$  and  $f_w$  losses. A substantial difference between the models is observed.

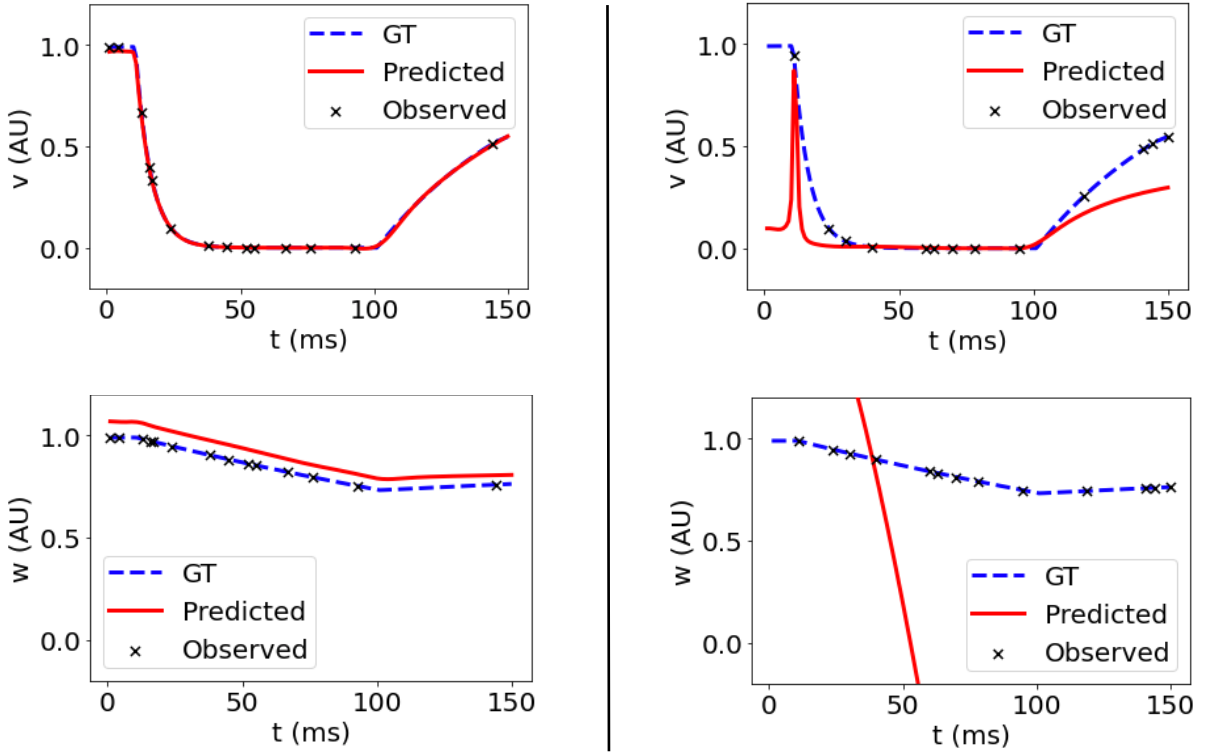


**Figure 3.6:**  $v$  and  $w$  estimation from full model (left) and reduced model (right).

### 3.1.2. Parameter Estimation (Inverse Solution)

To assess parameter estimation performance, Figure 3.7 shows a boxplot of the REs when estimating the parameters of interest individually and in pairs. Results for the reduced model are also included. For the full model, the diffusion coefficient  $D$  shows the best results with an RE close to zero even when estimated with other parameters. This is followed by parameters  $\tau_r$  and  $\tau_o$ , which also achieved a low RE in the 0.2 – 0.4 range. Finally,  $\tau_{si}$  was estimated with an error slightly higher than the previous two;  $\tau_d$  showed the poorest estimation with an RE of around 0.7. In most cases the results are slightly worse for the reduced model.  $D$  is estimated with the same accuracy,  $\tau_r$  and  $\tau_o$  are in the range of 0.2 – 0.6 RE,  $\tau_{si}$  has slightly worse RE, and  $\tau_d$  performs slightly better, around 0.5 RE. There is a total 9% increase in mean RE compared to the full model. There is also more variability, as observed in Figure 3.7.

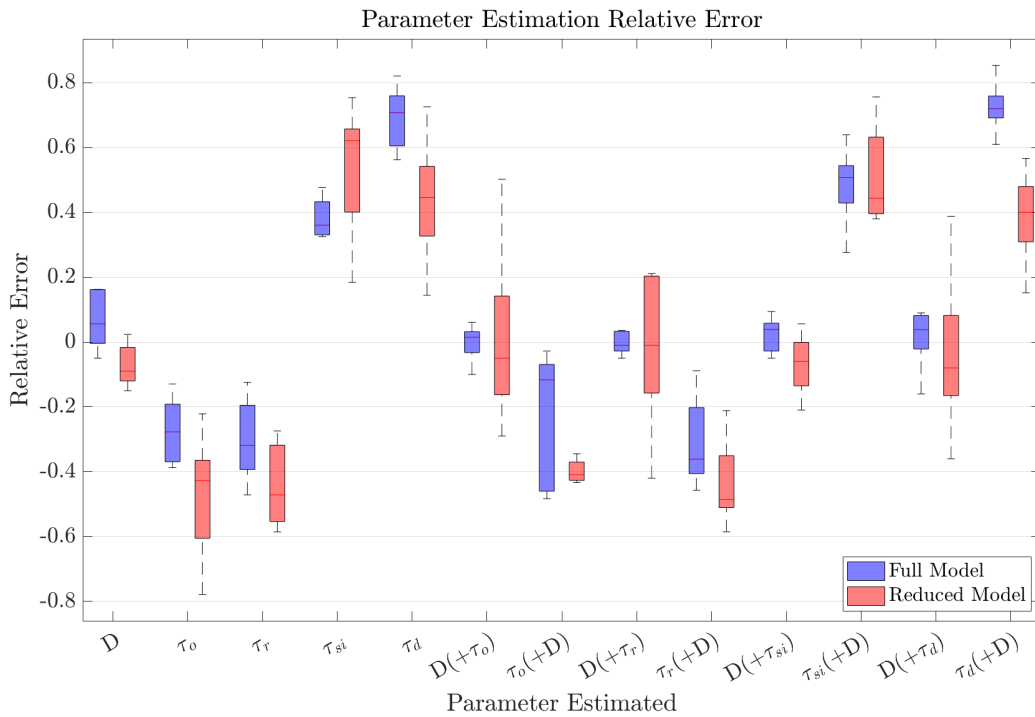


**Figure 3.7:** Parameter estimation RE boxplot for full and reduced models. The value in parenthesis is that estimated in pair with the actual value of interest outside the parenthesis.

The RMSE is very low in all cases (Figure 3.8). Performance is similar between all parameters and models in the  $10^{-3}$  range. There is a trivial 2% decrease in mean RMSE error in the reduced model with respect to the full one.

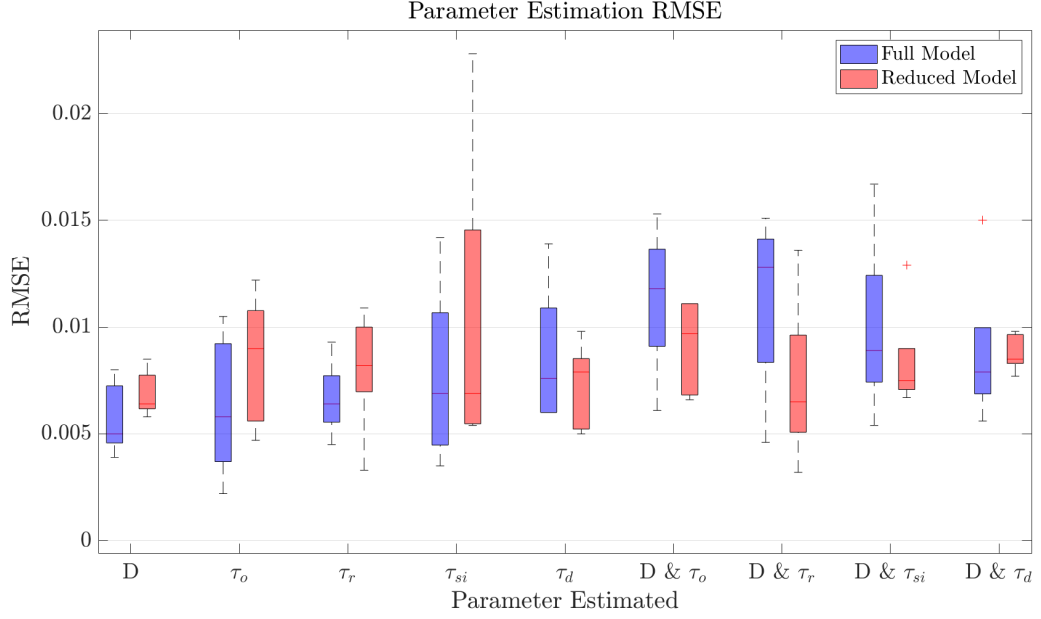


**Figure 3.8:** Parameter estimation RMSE boxplot for full and reduced models.

Figure 3.9 establishes that no correlation between RMSE and RE for both the full and reduced model is observed in any case.

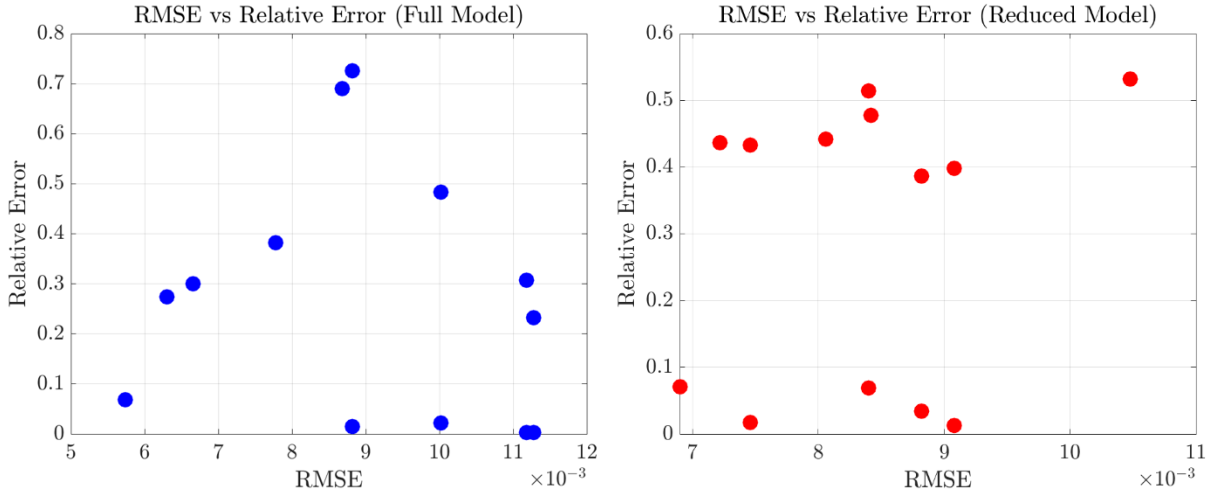


**Figure 3.9:** RMSE vs RE plot for full (left) and reduced (right) model.

### 3.2. Experimental Data

The EP-PINNs identified the effects in APD of Nifedipine and E-4031, from the optical mapping data (Figure 3.10). The EP-PINNs correctly predicted an increased APD under the effects of E-4031 with a  $APD_{90} = 19.88$  and  $APD_{50} = 13.10$  for the baseline, and  $APD_{90} = 21.50$  and  $APD_{50} = 13.20$  under the E-4031 effects. They also detected a significant increase in parameters  $\tau_r$  and  $\tau_o$  with respect to the baseline with  $p$ -values of  $p < 10^{-4}$ . The two-tailed t-test to check that  $\tau_{si}$  and  $\tau_d$  remained unchanged gave  $p$ -values of  $p = 0.32$  and  $p = 0.99$ , respectively. Both changes are non-significant; there is no evidence that the parameters changed between baseline and experimental measurements. For Nifedipine, the EP-PINNs identified a shorter APD associated with increased  $\tau_{si}$  with respect to baseline. The

APD measurements are  $APD90 = 19.58$  and  $APD50 = 11.93$  for the baseline, and  $APD90 = 17.37$  and  $APD50 = 8.69$  under the Nifedipine effects. However, the increased  $\tau_{si}$  was not statistically significant as the  $p$ -value for the t-test was  $p = 0.11$  ( $p > 0.05$ ). Nevertheless, the other parameters,  $\tau_r$ ,  $\tau_o$ , and  $\tau_d$ , gave  $p$ -values of  $p = 0.17$ ,  $p = 0.51$ , and  $p = 0.26$ , respectively, suggesting no significant difference in these parameters between baseline and experiment.

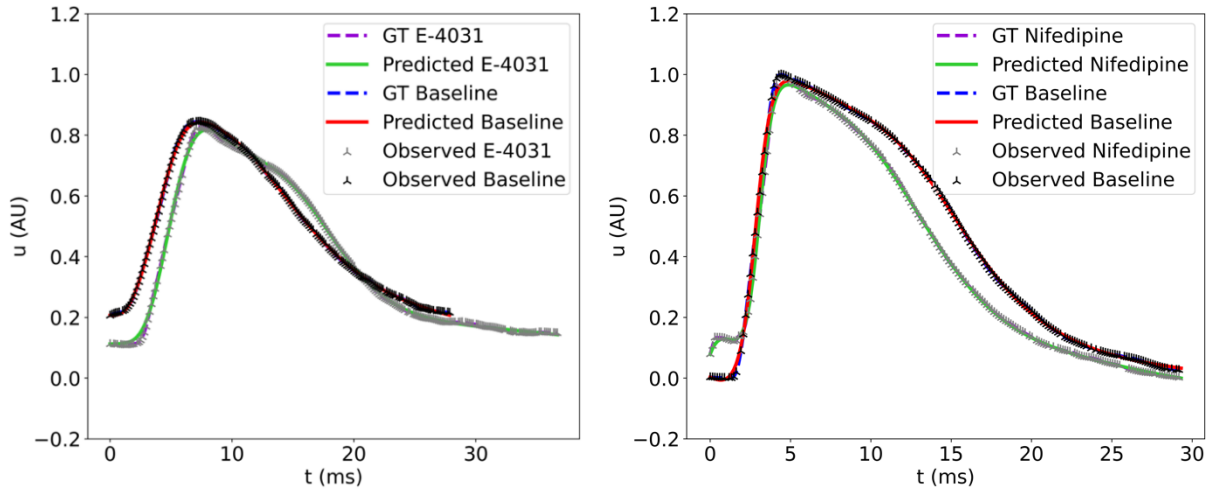


**Figure 3.10:** EP-PINNs estimations of the APs for E-4031 (left) and Nifedipine (right), including GT data.

## 4. Discussion:

The promising forward solution results show very low RMSE errors, robust-to-low and moderate noise levels, and solid with very low data availability. For the parameter estimation on the synthetic data, the RMSE resembles that of the forward model, and the RE was primarily low, but varied between parameters. On the experimental data, statistically significant changes in the relevant parameters were found for E-4031 but few for Nifedipine.

### 4.1. Synthetic Data

#### 4.1.1. Forward Solution

The EP-PINNs solved the Fenton-Karma model, accurately reproducing APs with a low RMSE error. EP-PINN accuracy was unaffected by the initialisation side (Figure 3.2) as the RMSE in both cases was similar (only a  $9 \times 10^{-4}$  difference). The model is invariant to initialisation from any side. The fact that the performance is unaffected by the side of the initialisation, indicates that the EP-PINNs follow properly the Fenton-Karma model.

The EP-PINNs were also tested in the presence of noise, as well as restrictions to data points and losses  $f_v$  and  $f_w$ . The network holds notably well until altered by noises of  $\sigma > 0.15$ . Higher noises were tested to observe how much the network could handle, and elevated noise levels of  $\sigma = 0.5$  gave noisy and inaccurate APs. The EP-PINNs are reliable even in the presence of some noise ( $\sigma < 0.15$ ) thanks to the particular loss function they are trained on, including  $L_f$  (physical-laws consistency loss). Louder noises (i.e.,  $\sigma = 0.9$ ) gave inaccurate APs as expected, but such a dataset would be immediately discarded as it would contain no reliable information on the AP.

Regarding the restriction to sampled data points in training, the EP-PINNs held exceptionally well up until  $\sim 100$  training data points, only 0.7% of the available data. This is important for clinical applications as the network might not have access in practice to an extensive dataset due to the difficulty of acquiring a highly sampled dataset of this kind. The great results with reduced data are due to the use of PINNs rather than regular NNs. Standard NNs learn only from data and therefore require large amounts to achieve accurate results. PINNs introduce problem-specific physical restrictions to the loss function, allowing it to be trained with fewer data.

When restricted to  $f_v$  and  $f_w$  losses, Figure 3.5 shows no noticeable difference in RMSE in both tests. The model can apparently be solved with the same efficacy with only the loss of  $f_u$ , suggesting that this loss and the data contain enough information for AP recreation even when subjected to noise and low sampled data. Omitting  $f_v$  and  $f_w$  losses reduces the burden to the network, accelerating training, requiring less data, and creating a simpler model without compromising results (RMSE). However, the EP-PINN does not converge to a solution for  $v$  and  $w$  when restricting access to their losses (Figure 3.6). It should be considered case by case if an accurate estimation of  $v$  and  $w$  is needed. If it is, one cannot train the EP-PINN without  $f_v$  and  $f_w$  losses.



#### 4.1.2. Parameter Estimation (Inverse Solution)

Parameter estimation is most relevant to clinical applications and to this study. Successful estimation of the Fenton-Karma parameters permits a detailed study of AAD action as the estimated parameters directly affect the  $J_{fi}(u; v)$ ,  $J_{so}(u)$  and  $J_{si}(u; w)$  currents which are homologous to the total  $\text{Na}^+$ ,  $\text{K}^+$ , and  $\text{Ca}^{2+}$  currents. The results demonstrate that the EP-PINNs successfully estimate most Fenton-Karma parameters with a very low RMSE (Figure 3.8).

Regarding parameter estimations, the poor performance of  $\tau_d$  was expected since Herrero Martin et al. (2022) have shown that this parameter (analogous to parameter  $a$  in their study using the Aliev-Panfilov model) hardly affects AP shape and is thus difficult to estimate from the data [2] (See also Figure 1.3). Parameters  $\tau_r$  and  $\tau_o$  evidently have a more significant effect on AP shape and duration than  $\tau_{si}$  and  $\tau_d$ . Therefore, the EP-PINNs can fit the APs even with  $\tau_{si}$  and  $\tau_d$  estimations not very close to the GT values. However,  $\tau_r$  and  $\tau_o$  need a more accurate estimation to fit the AP properly due to their considerable effect on AP shape and duration. All parameters except  $\tau_{si}$  were estimated with the same accuracy individually and in pairs, presumably due to the accurate estimation of  $D$ .

When restricted to  $f_v$  and  $f_w$  losses, AP reconstruction was similar (only a 2% RMSE difference). However, the 9% increase in mean RE suggests that a complete model estimates parameters slightly better. Therefore, it should be decided on a case-by-case basis whether the 20% reduction in training time is worth the 9% compromise on accuracy. This should also depend on the parameter of interest as performance varies between them.

There is no correlation between RMSE and RE (Figure 3.9), indicating that EP-PINNs minimise RMSE even when the Fenton-Karma parameters are incorrect, which is not ideal. The EP-PINNs would benefit from modifications enforcing realistic parameters, such as adding penalties when EP-PINNs estimate highly unreasonable values. Another option is moving to a probabilistic model where prior probabilities are entered into the network, enabling it to sample the parameters from a realistic distribution.

## 4.2. Experimental Data

The EP-PINNs correctly estimated the effect of the AADs (Figure 3.10) and APD measurements. Nifedipine significantly shortened the APD, as observed from the large difference in APD90 and APD50 measurements. The longer APD in E-4031 with respect to the baseline is more subtle, comprising rather a change in shape. The APD90 measurement suggests a longer APD, but the tiny difference in APD50 suggests a larger plateau phase followed by a steeper fall (Figure 3.10).

Regarding parameter estimation, the results for E-4031 were remarkable. The EP-PINNs identified both an increase in  $\tau_r$  and  $\tau_o$  and no change in  $\tau_{si}$  and  $\tau_d$ . Conversely, for Nifedipine they correctly detected no change in  $\tau_r$ ,  $\tau_o$ , and  $\tau_d$ , and no significant change in  $\tau_{si}$  which should have increased with respect to the baseline. Several reasons explain this difference. First,  $\tau_{si}$  has minimal effect in APD compared to  $\tau_r$  and  $\tau_o$  (Figure 1.3); therefore, the EP-PINNs need a more accurate prediction of  $\tau_r$  and  $\tau_o$  than  $\tau_{si}$  to achieve a good AP estimation. Second, the experimental measurements are noisy and have artefacts, which,

despite the EP-PINNs robustness to mild noise, affects the results. Nevertheless, these promising results allow for the estimation of most Fenton-Karma parameters for different individuals from clinical data, which would lead to individualised AAD treatment. More drugs should be tested on the EP-PINNs to achieve a complete picture of parameter estimation from clinical data.

### 4.3. Further Improvements

Membrane potential  $u$ , input to EP-PINNs, is not clinically measured. The EP-PINNs should be adapted to accept electrical potential inputs, measurable by electrograms [36]. This study observed the AP propagation through a 1D cable; it should be further scaled to 3D geometries resembling the human atrium. However, this may substantially increase computational-resource requirements. Further, cardiac models more sophisticated than the Fenton-Karma one could be implemented, perhaps perfectly representing  $\text{Na}^+$ ,  $\text{K}^+$ , and  $\text{Ca}^{2+}$  currents. Regarding experimental data, more drugs should be tested. Finally, despite the EP-PINNs' tolerance to some noise, a weighted loss function could be introduced, with the physical laws' loss term ( $L_f$ ) being more influential than the data loss term ( $L_{data}$ ) for noisy datasets.

## 5. Conclusion

This project coupled EP-PINNs with the Fenton-Karma mathematical heart model to estimate fundamental EP cardiac properties, as a means of personalising and thereby improving treatment and diagnosis of arrhythmias like AF. The EP-PINNs predicted AP propagation and estimated model parameters with high accuracy for synthetic and experimental data. Hopefully, this study will inspire further research on EP-PINNs combined with the Fenton-Karma model to improve the quality of life of those suffering from arrhythmias, particularly AF.

## 6. References

- [1] F. Fenton and A. Karma, "Vortex dynamics in three-dimensional continuous myocardium with fiber rotation: Filament instability and fibrillation a...", 1998. [Online]. Available: <http://ojps.aip.org/chaos/chocr.jsp>
- [2] C. Herrero Martin *et al.*, "EP-PINNs: Cardiac Electrophysiology Characterisation Using Physics-Informed Neural Networks," *Frontiers in Cardiovascular Medicine*, vol. 8, p. 2179, Feb. 2022, doi: 10.3389/FCVM.2021.768419/BIBTEX.
- [3] R. R. Aliev and A. v. Panfilov, "A simple two-variable model of cardiac excitation," *Chaos, Solitons & Fractals*, vol. 7, no. 3, pp. 293–301, Mar. 1996, doi: 10.1016/0960-0779(95)00089-5.
- [4] "Arrhythmia - NHS." <https://www.nhs.uk/conditions/arrhythmia/> (accessed Dec. 23, 2021).
- [5] S. Khurshid *et al.*, "Frequency of Cardiac Rhythm Abnormalities in a Half Million Adults," *Circulation: Arrhythmia and Electrophysiology*, vol. 11, no. 7, Jul. 2018, doi: 10.1161/CIRCEP.118.006273.
- [6] L. M. Haegeli and H. Calkins, "Catheter ablation of atrial fibrillation: an update," *European Heart Journal*, vol. 35, no. 36, pp. 2454–2459, Sep. 2014, doi: 10.1093/EURHEARTJ/EHU291.
- [7] J. Xu, J. G. Y. Luc, and K. Phan, "Atrial fibrillation: review of current treatment strategies," *Journal of Thoracic Disease*, vol. 8, no. 9, p. E886, 2016, doi: 10.21037/JTD.2016.09.13.
- [8] K. Golaszewska, E. Harasim-Symbor, A. Polak-Iwaniuk, and A. Chabowski, "Serum Fatty Acid Binding Proteins as a Potential Biomarker in Atrial Fibrillation", doi: 10.26402/jpp.2019.1.11.
- [9] E. J. Benjamin, P. A. Wolf, R. B. D'Agostino, H. Silbershatz, W. B. Kannel, and D. Levy, "Impact of Atrial Fibrillation on the Risk of Death," *Circulation*, vol. 98, no. 10, pp. 946–952, Sep. 1998, doi: 10.1161/01.CIR.98.10.946.
- [10] Johnson & Johnson Medical, "How is Atrial Fibrillation characterized?" <https://getsmartaboutafib.net/en-EMEA/hcp/atrial-fibrillation/what-is-atrial-fibrillation> (accessed Dec. 26, 2021).
- [11] G. Cheniti *et al.*, "Atrial fibrillation mechanisms and implications for catheter ablation," *Frontiers in Physiology*, vol. 9, no. OCT, p. 1458, Oct. 2018, doi: 10.3389/FPHYS.2018.01458/BIBTEX.
- [12] "Atrial fibrillation - Symptoms and causes - Mayo Clinic." <https://www.mayoclinic.org/diseases-conditions/atrial-fibrillation/symptoms-causes/syc-20350624> (accessed Dec. 27, 2021).
- [13] "Catheter Ablation | NHLBI, NIH." <https://www.nhlbi.nih.gov/health-topics/catheter-ablation> (accessed Dec. 24, 2021).
- [14] A. N. Ganesan *et al.*, "Long-term outcomes of catheter ablation of atrial fibrillation: a systematic review and meta-analysis," *J Am Heart Assoc*, vol. 2, no. 2, 2013, doi: 10.1161/JAHA.112.004549.
- [15] H. Calkins *et al.*, "2017 HRS/EHRA/ECAS/APHRS/SOLAECE expert consensus statement on catheter and surgical ablation of atrial fibrillation: executive summary," *Journal of Interventional Cardiac Electrophysiology*, vol. 50, no. 1, p. 1, Oct. 2017, doi: 10.1007/S10840-017-0277-Z.
- [16] J. McKenna, "Atrial Fibrillation Costs: Tests, Medications, Procedures." <https://www.webmd.com/heart-disease/atrial-fibrillation/costs-of-atrial-fibrillation> (accessed Dec. 24, 2021).

- [17] M. C. Sanguinetti and P. B. Bennett, "Antiarrhythmic drug target choices and screening," *Circulation Research*, vol. 93, no. 6, pp. 491–499, Sep. 2003, doi: 10.1161/01.RES.0000091829.63501.A8.
- [18] M. Varela, M. A. Colman, J. C. Hancox, and O. v. Aslanidi, "Atrial Heterogeneity Generates Re-entrant Substrate during Atrial Fibrillation and Anti-arrhythmic Drug Action: Mechanistic Insights from Canine Atrial Models," *PLoS Computational Biology*, vol. 12, no. 12, Dec. 2016, doi: 10.1371/JOURNAL.PCBI.1005245.
- [19] S. Nattel and D. Dobrev, "Controversies about Atrial Fibrillation Mechanisms: Aiming for Order in Chaos and Whether it Matters," *Circulation Research*, vol. 120, no. 9, pp. 1396–1398, Apr. 2017, doi: 10.1161/CIRCRESAHA.116.310489.
- [20] K. R. DeMarco and C. E. Clancy, "Cardiac Na Channels: Structure to Function," *Curr Top Membr*, vol. 78, p. 287, 2016, doi: 10.1016/BS.CTM.2016.05.001.
- [21] M. Grunnet, "Repolarization of the cardiac action potential. Does an increase in repolarization capacity constitute a new anti-arrhythmic principle?," *Acta Physiologica*, vol. 198, no. SUPPL. 676, pp. 1–48, Feb. 2010, doi: 10.1111/J.1748-1716.2009.02072.X.
- [22] P. A. Iaizzo and T. G. Laske, *Handbook of Cardiac Anatomy, Physiology, and Devices*. 2005. Accessed: Dec. 28, 2021. [Online]. Available: <https://antivirus.uclv.edu.cu/update/libros/Biomedical%20and%20Life%20Sciences/Handbook%20of%20Cardiac%20Anatomy%2C%20Physiology%2C%20and%20Devices%20-%20Paul%20A.%20Iaizzo%2C%203rd%20ed.%202015%20-%20978-3-319-19464-6.pdf>
- [23] X. Wei, S. Yohannan, and J. R. Richards, "Physiology, Cardiac Repolarization Dispersion and Reserve," *StatPearls*, Apr. 2021, Accessed: Dec. 27, 2021. [Online]. Available: <https://www.ncbi.nlm.nih.gov/books/NBK537194/>
- [24] G. Ikonnikov and D. Yelle, "Physiology of cardiac conduction and contractility | McMaster Pathophysiology Review." <http://www.pathophys.org/physiology-of-cardiac-conduction-and-contractility/> (accessed Dec. 27, 2021).
- [25] R. H. Clayton *et al.*, "Models of cardiac tissue electrophysiology: progress, challenges and open questions," *Prog Biophys Mol Biol*, vol. 104, no. 1–3, pp. 22–48, Jan. 2011, doi: 10.1016/J.PBIOMOLBIO.2010.05.008.
- [26] B. Marr, "How Much Data Do We Create Every Day? The Mind-Blowing Stats Everyone Should Read," May 21, 2018. Accessed: Dec. 29, 2021. [Online]. Available: <https://www.forbes.com/sites/bernardmarr/2018/05/21/how-much-data-do-we-create-every-day-the-mind-blowing-stats-everyone-should-read/?sh=1c69c8d960ba>
- [27] B. Bavarian, "Special Section on Neural Networks for Systems and Control Introduction to Neural Networks for Intelligent Control," *IEEE Control Systems Magazine*, vol. 8, no. 2, pp. 3–7, 1988, doi: 10.1109/37.1866.
- [28] H. Yi, S. Shiyu, X. Duan, and Z. Chen, "A study on Deep Neural Networks framework," *Proceedings of 2016 IEEE Advanced Information Management, Communicates, Electronic and Automation Control Conference, IMCEC 2016*, pp. 1519–1522, Feb. 2017, doi: 10.1109/IMCEC.2016.7867471.
- [29] "NN SVG." <http://alexlenail.me/NN-SVG/index.html> (accessed Dec. 29, 2021).
- [30] M. Raissi, P. Perdikaris, and G. E. Karniadakis, "Physics-informed neural networks: A deep learning framework for solving forward and inverse problems involving nonlinear partial differential equations," *Journal of Computational Physics*, vol. 378, pp. 686–707, Feb. 2019, doi: 10.1016/j.jcp.2018.10.045.
- [31] I. R. Efimov, V. P. Nikolski, and G. Salama, "Optical imaging of the heart," *Circulation Research*, vol. 95, no. 1, pp. 21–33, Jul. 2004, doi: 10.1161/01.RES.0000130529.18016.35.

- [32] R. A. Chowdhury *et al.*, “Concurrent micro- to macro-cardiac electrophysiology in myocyte cultures and human heart slices,” *Scientific Reports* 2018 8:1, vol. 8, no. 1, pp. 1–13, May 2018, doi: 10.1038/s41598-018-25170-9.
- [33] A. M. Goodman, R. A. Oliver, C. S. Henriquez, and P. D. Wolf, “A membrane model of electrically remodelled atrial myocardium derived from in vivo measurements,” *EP Europace*, vol. 7, no. s2, pp. S135–S145, Jan. 2005, doi: 10.1016/J.EUPC.2005.04.010.
- [34] L. Lu, X. Meng, Z. Mao, and G. E. Karniadakis, “DeepXDE: A deep learning library for solving differential equations,” *SIAM Review*, vol. 63, no. 1, pp. 208–228, 2021, doi: 10.1137/19M1274067.
- [35] T. K. Kim, “T test as a parametric statistic,” *Korean Journal of Anesthesiology*, vol. 68, no. 6, p. 540, Dec. 2015, doi: 10.4097/KJAE.2015.68.6.540.
- [36] D. D. C. de Sa *et al.*, “Electrogram fractionation: the relationship between spatiotemporal variation of tissue excitation and electrode spatial resolution,” *Circ Arrhythm Electrophysiol*, vol. 4, no. 6, pp. 909–916, Dec. 2011, doi: 10.1161/CIRCEP.111.965145.